http://eprints.gla.ac.uk/149974/

Dimension- and shape-dependent thermal transport in nano-patterned thin films investigated by scanning thermal microscopy

Yunfei Ge, Yuan Zhang, Jonathan M. R. Weaver, Phillip S. Dobson*

Email: Phil. Dobson@glasgow.ac.uk

Address: School of Engineering, Rankine Building, University of Glasgow, UK, G12 8LT

Scanning Thermal Microscopy (SThM) is a technique which is often used for the measurement of the thermal conductivity of materials at the nanometre scale. The impact of nano-scale feature size and shape on apparent thermal conductivity, as measured using scanning thermal microscopy, has been investigated. To achieve this, our recently developed topography-free samples with 200 nm and 400 nm wide gold wires (50 nm thick) of length of 400 – 2500 nm were fabricated and their thermal resistance measured and analyzed. This data was used in the development and validation of a rigorous but simple heat transfer model that describes a nanoscopic contact to an object with finite shape and size. This model, in combination with a recently proposed thermal resistance network, was then used to calculate the SThM probe signal obtained by measuring these features. These calculated values closely matched the experimental results obtained from the topography-free sample. By using the model to analyze the dimensional dependence of thermal resistance, we demonstrate that feature size and shape has a significant impact on measured thermal properties that can result in a misinterpretation of material thermal conductivity. In the case of a gold nanowire embedded within a Silicon Nitride matrix it is found that the apparent thermal conductivity of the wire appears to be depressed by a factor of twenty from the true value. These results clearly demonstrate the importance of knowing both probe-sample thermal interactions and feature dimensions as well as shape when using SThM to quantify material thermal properties. Finally, the new model is used to identify the heat flux sensitivity, as well as the effective contact size of the conventional SThM system used in this study.

Introduction

Scanning thermal microscopy (SThM) is a technique that combines atomic force microscopy (AFM) with an integrated thermal sensor[1,2]. It is well established and, thanks to its high spatial resolution and thermal sensitivity, has been widely used to measure device temperatures[3,4] and material thermal properties[5–7] at the nanoscale. SThM probes can be employed as thermometers when used with negligible self-heating (passive mode). However, it should be noted that probe temperature is only proportional to sample temperature due to the thermal interface resistance at the tip-sample contact, R_{int}, which dominates temperature measurement[5,8–10]. When operated in active mode (self-heated probe), SThM can distinguish between materials of differing thermal conductivity by measuring the degree of cooling the tip experiences as a result of contact with each material. In both modes, the assumption that the tip-sample thermal interface resistance does not vary is used to allow the temperature and thermal spreading resistance of the sample to be quantified[5,11,8]. The interpretation of measurements made in active mode is more complex than passive mode. This is due to the fact that measured thermal spreading resistance (R_s) is influenced by sample structure as well as material thermal properties. Although material thermal properties can be influenced when features are of similar dimensions to the mean free path of phonons in the system, geometries larger than this can still significantly impact on the spreading resistance of an object even though the material thermal properties remain the same as bulk. This makes quantitative measurement of material thermal properties using SThM very challenging and an area that requires further study.

Whether the probe is driven using an AC or DC signal, the process of determining R_s is the same: build a thermal resistance network based on heat transfer mechanisms between the probe and sample, define the contribution of each thermal element, and finally extract R_s from this network[12]. More specifically, the thermal resistance of the probe[5,11,8], thermal interfacial resistance and the effect of air R_{air}[6,13,14] can all be determined by either experiment or numerical modelling, or, in the case of air, be eliminated completely by employing a vacuum system. Additional complications from the water meniscus as well as radiation have been proved to be negligible and are therefore ommited[12,15,16].

After acquiring the thermal spreading resistance of a sample, it is common practice to convert this value into material thermal conductivity. Recent work on SThM measurement demonstrates how thermal conductivity can be interpreted from various kinds of samples. Menges *et al.*[7] used a self-heated doped silicon probe successfully determining the thermal conductivity of graphene films on different substrates. This was achieved by treating the tip-sample thermal interaction as a

nanoscopic constriction in contact with a half-space surface. In this case, thermal spreading resistance within the graphene film could be expressed using a 1D heat transfer equation without taking the lateral dimensions of the graphene sheet into account. The same "nanoscopic to half-space" conduction model has also been adopted to characterize hafnium oxide (HfO_2) and SiO_2 thin films[6]. Beyond simple thin films, Puyoo *et al.*[11,17] utilized SThM in 3ω mode method to carry out accurate measurement of individual silicon nanowires. In this instance, the dimensions of the nanowire played an important role in the interpretation of thermal conductivity. Due to the similar dimensions of the nanowires and the probe-sample contact size, thermal conductivity could still be extracted by modelling thermal conduction within the sample as 1D heat transfer. Investigation of carbon nanotubes has been carried out using a similar "nanoscopic to 1D structure" conduction model[18]. Recently, work by Hwang *et al.*[19] investigating suspended graphene disks revealed that it was essential to consider both sample dimensions and SThM probe contact size[19,20] when the sample was larger than the probe contact size but too small to be considered as infinite. Although this scenario is more complicated than the previous two, thermal conduction within the graphene could still be considered as 1D by employing spherical coordinates, which are appropriate for the thermal conduction profile, the shape of the graphene disks and the probe-sample circular contact.

However, the 1D model reaches its limits when there is an inconsistency between the thermal diffusion profile at the nanoscopic contact and the finite shape of a sample feature. Following the naming scheme above, this scenario can be called "nanoscopic to finite dimension" conduction. Rectangular thin films are commonly employed in several areas including VLSI interconnects[21], graphene nanoribbons[22,23] and research into nanoscale heat transfer[24]. However measuring these rectangular structures using SThM is always accompanied by the complexity of modelling and solving heat transfer problems beyond 1D[25]. Thermal spreading resistance of rectangles has been discussed and summarized by Yovanovich[26,27], however, this work only considered rectangular heat sources on a half-space or heat sources with the same shape as the substrate.

In the work presented here, we propose a combined-fin (CF) model to describe the thermal spreading resistance of rectangular thin films in contact with a SThM probe, avoiding the need for complex multi-dimensional heat transfer analysis. This model is then verified against measurements and used to investigate finite-shaped thin films of a commonly used material, gold. Conventional patterned samples, integrating multiple materials, typically exhibit significant topography leading to artifacts in the SThM signal due to the variation of tip-sample contact area[12,28]. This results in data that is inaccurate and open to misinterpretation. To avoid the issue, we have employed a recently developed approach to fabricate topography-free samples[29]. These samples have enabled us to make the first systematic demonstration illustrating the effect of feature dimensions on thermal spreading resistance as measured by SThM independent of topographic artefacts. The feature spreading resistance was calculated from SThM probe temperature by employing the thermal resistance network proposed in our recent work[30]. The resulting values were then used to validate the CF model. This allowed the CF model to be employed to identify the threshold, at which the spreading resistance is significantly influenced by shape. Finally, this information was used to analyze the experimental data, providing a measurement of effective probe-sample contact size, as well as the thermal spatial resolution of the SThM method employed.

Methods

The topography-free sample was fabricated as described in our previous work[29], however it will be briefly summarised here. 50 nm thick gold wires were defined and fabricated on a piece of GaAs substrate by electron beam lithography (EBL) followed by evaporation of metal and liftoff. 500 nm of low stress SiN_x was then deposited on the sample by inductively coupled plasma chemical vapour deposition (ICP-CVD), followed by a 100 μm thick spin-coated layer of SU-8 acting as an adhesive to a quartz slide. Finally, the GaAs substrate was removed using a mixture of citric acid with H_2O_2, exposing the gold and SiN_x. A typical complete pattern is illustrated in Figure 1 (a) and (b) with optical microscopy and scanning electron microscopy (SEM) images. The pattern consists of a gold wire located in a 1 μm gap between two 5 μm × 5 μm gold pads, permitting easy pattern location within the AFM using optical microscopy. Since the tip-sample contact area for the probes used is typically considered to be a circle having the same radius as the tip curvature[11,16,32], all gold wires were fabricated with dimensions greater than this to ensure complete tip-wire contact during measurement. The pattern was scanned using the SThM method and compensated cantilever resistive thermal probe described elsewhere[33]. This probe has the same overall dimensions as the commonly used Kelvin NanoTechnology (KNT) probe[5,11,17,34,35], but incorporates design features to minimise thermal bending of the cantilever. In addition, the probe omits the two NiCr current limiters in series with the tip of the KNT probe, allowing Joule heating to be known more accurately. The apex radius was estimated to be the same as the tip radius of curvature (~ 50 nm)[15,16] and the temperature coefficient of resistance (α) was measured as 0.000961 K^{-1}.[29] The probe was used in contact mode under ambient conditions, and operated in constant power mode ($P = 1.02 \times 10^{-4}$ W) configured in a Wheatstone bridge. Any increase in electrical resistance was converted to temperature above ambient.
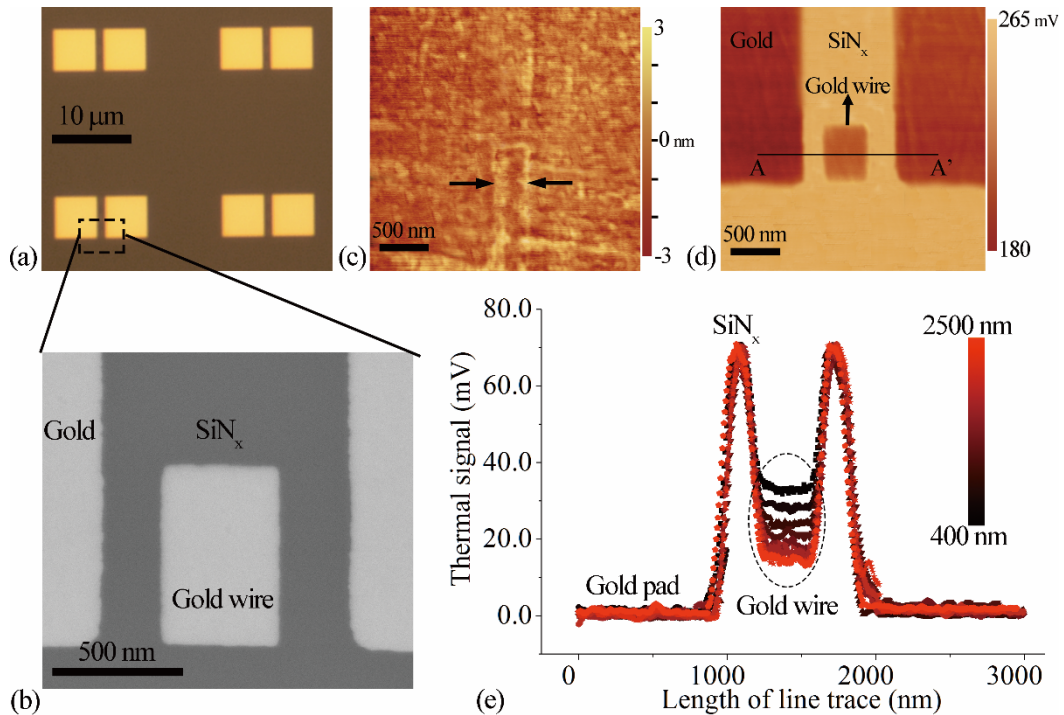

Figure 1 (a) Optical microscope image of the topography-free pattern, (b) SEM image of the indicated region showing a gold wire with 400 nm width and 700 nm length. (c) Simultaneously obtained SThM topographic and (d) thermal images of the 2.5 μm × 2.5 μm region. (e) Plot of thermal signal intensity at the line A-A' for 400 nm wide wires with the length varying from 400 nm to 2500 nm showing the variation of thermal contrast with wire length for the same material which might (wrongly) be interpreted as a change in the intrinsic thermal resistance of the film.

The topographic image obtained simultaneously with the SThM thermal image (Figure 1 (c)) shows that the root mean square roughness of the surface was 1.5 nm, and that the gold pattern could not be distinguished from the background SiN_x. The actual position of the gold wire is indicated by the two arrows. The topographic and thermal signals were recorded simultaneously using a Veeco Dimension 3100 AFM with a scan size of 3 μm × 3 μm, and resolution of 512 × 512 pixels. The scan speed was 0.5 Hz, guaranteeing the tip was in local thermal equilibrium at each pixel. No obvious topographically induced artifacts can be seen in the thermal image (Figure 1 (d)), greatly assisting the thermal analysis. A line trace at the mid-point of each wire (e.g. see A-A' in Figure 1 (d)) was used to extract data from each thermal scan. A series of 400 nm wide wires with length varying from 400 nm to 2500 nm were scanned, and their thermal intensities plotted in Figure 1 (e). In each

case, the data was offset so that the gold pads of each had the same thermal signal. It can be clearly seen that although the gold wires share the same material and thickness as the gold pads, their thermal signals are different, showing a strong, systematic dependence on their length. As the magnitude of the thermal signal is dependent on the thermal spreading resistance of the sample, this dimensional effect could result in misinterpretation of feature thermal conductivity, unless an appropriate model is employed for data analysis.

Results

The model was constructed based on a rectangular gold wire, with thickness t and width w, surrounded by SiN_x on all surfaces except for its top, which was exposed to air, as shown in Figure 2 (a). When a heated SThM probe contacted the centre of the gold wire, heat conducted through the body dissipating into the environment along its length through thermal conduction into the air (h_a) and substrate (h_s) as shown in Figure 2 (b). Heat loss from the interfaces with air and SiN_x will be far less than conduction within the gold wire, resulting in a Biot number much less than 0.01. This allows us to consider the gold wire as two joined fins[36]: a radial fin from the contact point (R_0) to the boundary of the y direction (R_1) (Figure 2 (c)) and a straight fin from the boundary of the radial fin to the boundary of the x direction (Figure 2 (d)).
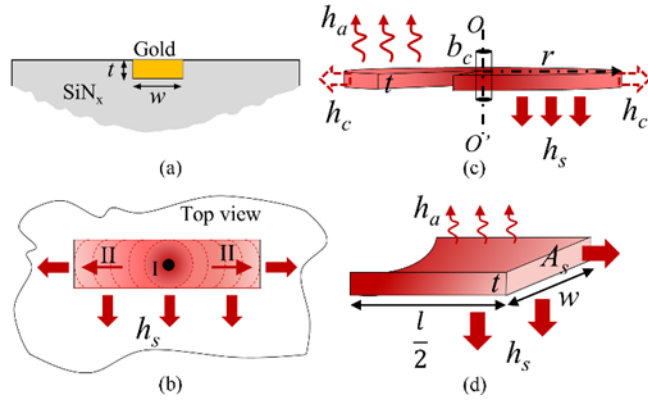

Figure 2 (a) Cross-section view of a gold wire on the topography-free sample, (b) schematic of heat transfer due to a nanoscopic contact (the black circle) at the center of a finite-dimension gold wire, (c) heat transfer mechanisms of the radial fin shown in spherical coordinates, and (d) heat transfer mechanisms of a straight fin connected with the radial fin defined in Cartesian coordinates.

A heat transfer equation expressing thermal diffusion in a radial fin can be written as

$$-kA\frac{dT}{dr}\Big|_r = -kA\frac{dT}{dr}\Big|_{r+dr} + h_aA_t(T - T_\infty) + h_sA_b(T - T_\infty) \qquad (1)$$

where k is the thermal conductivity of the gold, $A = 2\pi rt$ is the cross-section area at position r, $A_t = A_b = 2\pi r dr$ is the elemental area of the top and bottom surface respectively. h_a is estimated as 1×10^5 W/m²K from the work of Chen $et\ al.$[20], and h_s considers both the interfacial conductance and thermal diffusion within the substrate. To simplify the calculation, a dimensionless expression $\theta = \frac{T-T_\infty}{T_w-T_\infty}$, where T_∞ and T_w represent the temperature of contact area and ambient respectively, is used to substitute T as

$$r^2\frac{d^2\theta}{dr^2} + r\frac{d\theta}{dr} - \frac{(h_a+h_s)r^2}{kt}\theta = 0 \qquad (2)$$

which is a modified Bessel function with a general solution

$$\theta = C_1 I_0(mr) + C_2 K_0(mr) \qquad (3)$$

where $m = \sqrt{\frac{h_a+h_s}{kt}}$, I_0 and K_0 are zero order Bessel functions of first and second kind respectively, and C_1 and C_2 are integration constants.

As the radial fin will conduct heat into the straight fin at $r = R_1$ and inherit the temperature of the contact area at $r = R_0$, two boundary conditions of the radial fin are

$$1 = C_1 I_0(mR_0) + C_2 K_0(mR_0) \qquad (4)$$

$$h_c A_{R_1}\theta = -kA_{R_1}\frac{d\theta}{dr} \qquad (5)$$

4

where h_c is the equivalent thermal conductance per unit area at the edge of the radial fin due to the straight fin, which can be defined from its thermal resistance $(R_{straight})$[36]

$$R_{straight} = \frac{1}{\eta_f\left[R_1\frac{l}{2}h_a+(R_1+2t)\frac{l}{2}h_s\right]} \qquad (6)$$

where η_f is the straight fin efficiency and defined as $\eta_f = \tanh{(m_sL)}/m_sL$, in which $L = l/2 + t/2$ is the corrected length of the fin due to the existence of heat exchange with the SiN_x at the end of the straight fin, and $m_s = \sqrt{[h_s(\pi R_1 + 2t) + h_a\pi R_1]/k\pi R_1 t}$. Thus, the equivalent thermal conductance per unit area due to the straight fin is

$$h_c = \frac{1}{R_{straight}\frac{A_{R_1}}{2}} \qquad (7)$$

So far, thermal resistance of the radial fin can be determined as

$$R_{radial} = \frac{\theta_w}{q_f} \qquad (8)$$

where q_f, the heat transfer rate within the radial fin, can be defined as

$$q_f = -kA\frac{d\theta}{dr}\Big|_{r=R_0} = 2\pi kR_0 tm[C_2K_1(mR_0) - C_1I_1(mR_0)] \qquad (9)$$

To solve the thermal resistance, h_s, the thermal interfacial resistance between the gold and SiN_x, has to be determined. This was obtained by analysing the thermal resistance of the 5 μm × 5 μm gold pad measured in the same experiment. The thermal contrast of a pad of 5μm size or larger is found experimentally to be independent of pad size, so that this feature can be assumed to be a half space for the purposes of analysis. Its thermal resistance calculated as 3.42×10^4 K/W from[37]

$$R_{Au-pad} = \frac{1}{4k_{Au}b_c} - \frac{1}{4\pi k_{Au}t}\ln\left(\frac{2}{1+\frac{k_{Au}}{k_{SiN}}}\right) \qquad (10)$$

where the thermal conductivities of 50 nm thick gold and 500 nm thick SiN_x deposited using same method as in this work are taken to be $k_{Au} = 250$ W/mK[38] and $k_{SiN} = 10$ W/mK[39]. Note that the thermal conductivity of SiN_x is a strong function of stoichiometry and deposition conditions, but fortunately equation (10) is only a weak function of this value. For an extreme practical range of k_{SiN} ranging from 7-33 the value of R_{Au-pad} varies by only +6 to -19% from that obtained using the assumed value, thanks to the logarithm in the second term of equation (10). A change in the value of k_{Au} over a range of 10% gives a similar change in the value of R_{Au-pad}, as would a change in contact b_C to 100nm diameter. This provides a conservative estimate of the absolute variation in R_{Au-pad} to be expected in practice.

The same gold pad can be modelled as a radial fin, as described above, with infinite radius. In this case, the boundary condition at R_0 remains unchanged, but the edge boundary condition changes to

$$0 = C_1I_0(mr) + C_2K_0(mr) \text{ with } r \to \infty \qquad (11)$$

By equating these two calculations to each other, the thermal resistance h_s can be calculated to be 3.071×10^7 W/m²K. This value agrees with the thermal conductance between gold and dielectric materials determined in other work[40–42].
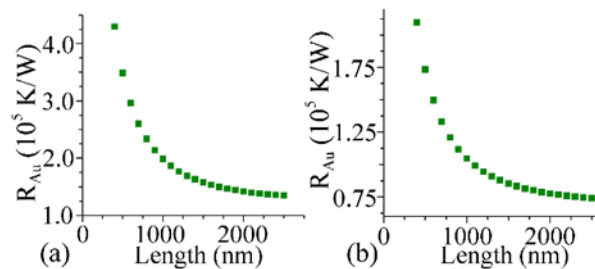

Figure 3   Thermal resistance of gold wires against their length in (a) 200 nm and (b) 400 nm width calculated from the CF model.

With all of the constants known, the thermal resistance(R_{Au}) of 200 nm (Figure 3 (a)) and 400 nm (Figure 3 (b)) wide gold wires with length ranging from 400 nm to 2500 nm can be calculated using the model. R_{Au} can be linked to measured probe temperature by taking into account thermal interactions between the probe and the sample using the lumped-system model proposed in our recent work[30]. This model accounts for the interactions between the probe and sample by dividing the probe into several lumped systems based on its shape and materials. As the original model was built for SThM probes used in passive mode, several modifications have been made in order to adapt it to the active probe. As shown in Figure 4, Joule heating power applied to the probe can be modelled as a current source ($I_{th} = P$). Thermal resistance of the gold wire is taken into account as R_s in series with thermal interfacial resistance $R_{tip\text{-}s}$, which changes depending on sample materials. Furthermore, thermal spreading resistance within the sample due to the air gap between the probe and the sample, marked as R_i^{sub}, can be considered to be a circular heat source on a half-space, $1/(4kb_c)$[10]. R_i^{SiN}, R_i^{pt}, and R_i^{air} are thermal resistances due to thermal conduction through the probe and air, and can all be considered to be the same as those in the original passive model. The only unknown value is $R_{tip\text{-}s}$, which can be determined experimentally as described later. In common with the original passive model, T_2 can be considered to be the average temperature of the platinum sensor above ambient (ΔT) due to the neglected contribution of T_1[30].
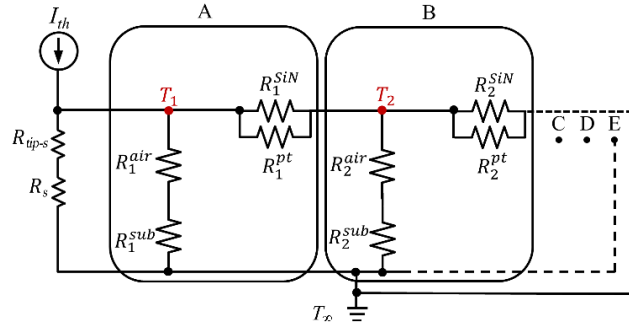

Figure 4 Lumped system model for probe working in active mode. A–E represent the lumped parts divided according to the probe's material and shape (A and B for the platinum tip, and C, D and E for the remaining parts). A detailed description of the model can be found in Ref.[30].

$R_{tip\text{-}Au}$ (i.e. $R_{tip\text{-}s}$ for a probe contacting gold) can be determined as 0.985×10^6 K/W by equating the experimentally measured probe temperature when in contact with the gold pad with the lumped-system model when R_s is the thermal resistance of gold pad as calculated previously. With the knowledge and the contact radius, as described above, the thermal boundary resistance between the platinum tip and the gold ($R_{b\text{-}Au}$) can be calculated as 7.736×10^{-9} m²K/W from $R_{tip-Au} = \frac{R_{b-Au}}{\pi(b_c)^2}$[43]. This is in agreement with values determined by other researchers[5,10,37,44].

The SThM probe temperature when in contact with the various gold wires can now be calculated by replacing R_s in the model above with R_{Au} as determined from the CF model. Experimentally, the probe temperature can be determined by considering the average thermal signal from a square of 18×18 pixels (similar to the area of contact) at the center of the thermal image of the gold wire. Both the modelled and measured SThM probe temperatures for the various wires are plotted in Figure 5. It can be seen that the trend of both curves show an excellent match, suggesting that thin films with finite dimensions measured using the SThM probes used in this work can be modelled as a radial fin connected to a straight fin. There is a small (~0.1 K) temperature discrepancy between the measured and modelled values and it is believed that this may be the result of the local environment becoming heated during the experiment, for example by the AFM laser or optical microscope illumination. This offset is present for all data points of Figure 5, but is most visible at large lengths, where the data and modelled data tend to horizontal.
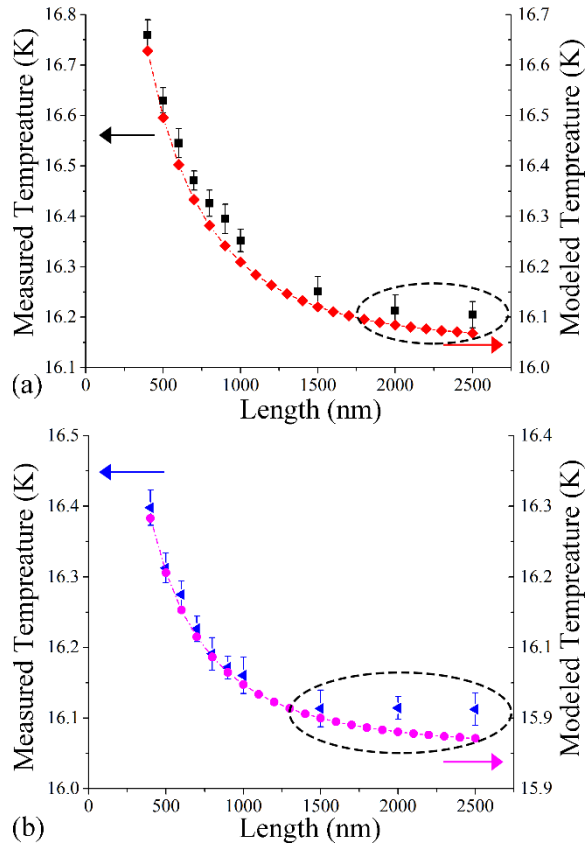
Figure 5 Plots of tip temperature from both measurement (black squares and blue triangles "Measured T") and thermal resistance network (red diamonds and purple circles "Modelled T") versus the length in (a) 200 nm wide and (b) 400 nm wide gold wires. The error bars in the experimental plot represent ±1 standard deviation of each 324 pixel averaged value.

Except for those points indicated by the dashed circles in both Figure 5 (a) and (b), the probe shows sensitivity to variations in thermal resistance caused by the wire dimensions. A comparison between the tip temperature and the calculated thermal resistance reveals that only variation in thermal resistance exceeding 9×10^3 K/W will result in a measurable deviation. The noise in this experiment comes from various sources, with sensor circuitry, variations in ambient conditions and residual sample topography all contributing[45]. The root-mean-square value of noise in this experiment is 0.038 K. This value however cannot be directly used to define the sensitivity of the probe to sample thermal resistance, since the sensitivity is dependent on the thermal interfacial resistance between the probe and sample, which changes with sample material. According to the argument proposed by Menges et al.[3], variation in heat flux (ΔQ) is more suitable for expressing the detection sensitivity. Here, by referring to the lumped-system model in Figure 4, ΔQ associated with a tip temperature change of 0.038 K can be determined as ~ 200 nW. This value is three orders larger than that obtained by Menges in their work (~ 100 pW), which may be attributed to their advanced "AC+DC" measurement strategy as well as their use of a high-vacuum system with electromagnetic shielding in a temperature stable lab.
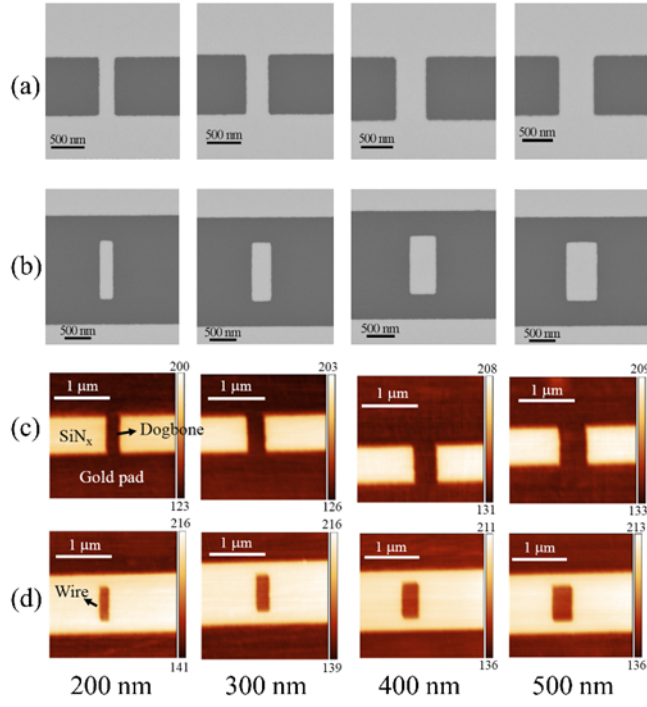
Figure 6 SEM images of row (a) "dogbone" patterns with width varying from 200 nm to 500 nm, and row (b) "fake dogbone" patterns with the same widths. Row (c) and (d) show SThM thermal maps of the "dogbone" and "fake dogbone" pattern respectively.

Another conclusion that can be drawn from this work is the impact the nanoscale feature shape has on quantitative thermal analysis using SThM if an appropriate model is not employed. To demonstrate the dimensional effect more intuitively, eqn (10) can be used to calculate the apparent thermal conductivity from the thermal resistance of wires with all dimensions. This tells us that for a wire 200 nm wide and 400 nm long (the largest thermal resistance considered here), the apparent thermal conductivity is 11.8 W/mK. This is over twenty times smaller than that of bulk Au, and is close to that of SiN_x. Since the gold wire is 50nm thick the real thermal conductivity of the wire will not be significantly affected by lateral confinement effects at this scale. Rather, the error in apparent thermal conductivity is due to the mode of thermal conduction out of the wire, which is a strong function of shape.

By considering the theoretical analysis of straight fins above, it can be observed that not only length and width, but also heat transfer at the boundaries will affect h_c. For gold wires with uniform geometry, the boundary condition at the end of the straight fin is thermal conduction with the surrounding SiN_x as described by h_c. However, if the straight fin is instead connected at its end to an ambient temperature heat sink, the calculation of h_c detailed above must be reconsidered. To study this an additional sample was designed to include a "dogbone" pattern in order to vary the boundary condition of the straight fin. As shown by the SEM images in Figure 6 (a), the "dogbone" consisted of 1 μm long gold wires connected to two gold pads at their ends. It should be noted that the wires and pads were written using EBL in a single layer, guaranteeing a continuous feature. Alongside this pattern, a similar set of isolated wires were produced, as shown in Figure 6 (b), sharing the same dimensions and material as the "dogbone" wires. However, these "fake dogbone" wires included a small gap between the wire and pads, with the intention of demonstrating the shape effect more clearly.

The thermal resistance of this new feature was calculated in a similar way to the wires described above with the difference that the 5 μm × 5 μm gold pad at each end was assumed to be a perfect heat sink at ambient temperature. Therefore, the boundary conditions could be written as

$$\epsilon_1 = T_1 - T_\infty \qquad (12)$$

$$\epsilon_2 = 0 \qquad (13)$$

where ϵ_1 and ϵ_2 are the excess temperature defined as $(T - T_\infty)$ at the edge of the radial fin and the straight fin respectively. This allows the heat transfer rate within the straight fin to be defined as

$$q_s = m_s k A \epsilon_1 \frac{\left(\cosh m\frac{l}{2} - \frac{\epsilon_2}{\epsilon_1}\right)}{\sinh m\frac{l}{2}} \qquad (14)$$

8

Thermal resistance of the straight fin in this condition is therefore

$$R'_{straight} = \frac{\epsilon_1}{q_s} \qquad (15)$$

Thus the thermal conductance per unit area at the edge of radial fin is

$$h'_c = \frac{1}{R'_{straight}A} \qquad (16)$$

Similar to the individual gold wires, thermal resistance of these features was determined and used as R_s in the lumped-system model, allowing the tip temperature to be calculated.

The experiment was carried out using the same SThM setup and settings as described previously. In addition to obtaining thermal scans of the "dogbone" patterns, the "fake dogbone" patterns were also imaged in order to demonstrate the shape effect more clearly and a comparison is shown in Figure 6 (c) and (d). It can be immediately seen that wires of the "dogbone" patterns exhibit a similar probe temperature to the gold pads. In addition, although the wires become wider, there is no strong width-dependence phenomenon present in their signal. In contrast, the isolated wires demonstrate a higher temperature than gold pads, indicating a larger thermal resistance.
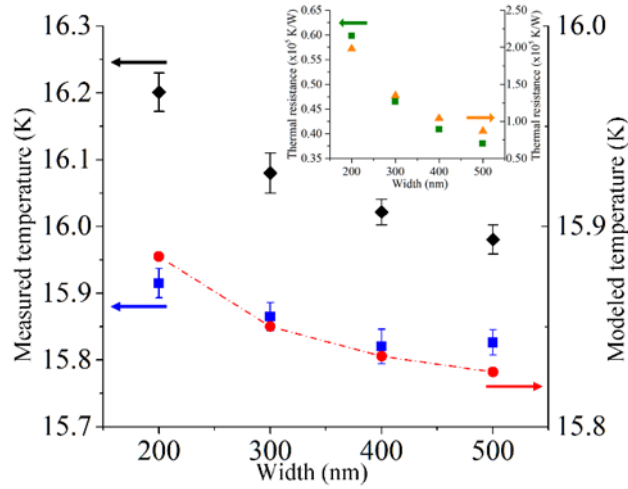

Figure 7 Plots of the SThM tip temperature when measuring the "Dogbone" pattern. Blue squares and red circles indicate the measured and modelled tip temperature of the "Dogbone". For comparison, the measured tip temperature on isolated wires is shown by black diamonds. The inset figure gives the plot of thermal resistance of the "Dogbone" pattern (green squares) and that of isolated wires (orange triangles).

The results from the experimentally measured SThM tip temperatures when in contact with "Dogbone" wires, together with the associated modelled values are shown in Figure 7 as blue squares and red circles respectively. From the simulation result, the trend of temperature can still be observed to follow the feature thermal resistance with changes in width (green squares in inset). However, the variation is small and can hardly be observed experimentally, especially when the measurement standard deviation is taken into account. In contrast, the probe temperature from isolated wires (black diamonds) demonstrates much stronger dependence on thermal resistance (orange triangles in inset) resulting in higher tip temperatures. This is in good agreement with Figure 7 where "Dogbone" patterns exhibit similar signals between gold pads and wires, while isolated wires show a clear difference between the two. The impact of changing the boundary conditions can be clearly seen. In addition, the same model described above can effectively describe both scenarios with only the simple replacement of boundary conditions.

Discussion

Based on the observations above, it can be stated that a detailed knowledge of a feature's dimensions and shape is essential if its thermal conductivity is to be reliably extracted from a measurement of its thermal resistance. However, the question remains as to whether this can be truly achieved for other, less constrained samples such as composite materials. For the probe and experimental setup used in this work, we can state that an object can be treated as a half-space if its thermal resistance deviates from bulk insufficiently to cause a change in heat flux larger than ~ 200 nW. More specifically, if considering the gold employed in this work, rectangular films with thermal resistance within 1.41×10^4 K/W of that exhibited by the gold pad (3.42×10^4 K/W) can be treated as a half-space. Figure 8 is a contour plot showing thermal resistance against the width and length of a gold wire. The areas shaded red represent gold wires that can be treated as a half space corresponding to a thermal

resistance smaller than 4.83×10^4 K/W. If we follow the convention that width is always equal to or smaller than length, we can state that all gold wires with width larger than 1100 nm can be analysed as a half-space, while any wire with width smaller than 750 nm must have dimensional effects taken into account (presented as the two dotted red lines). It should be noted that this plot is only valid for the materials and shapes considered in this work.
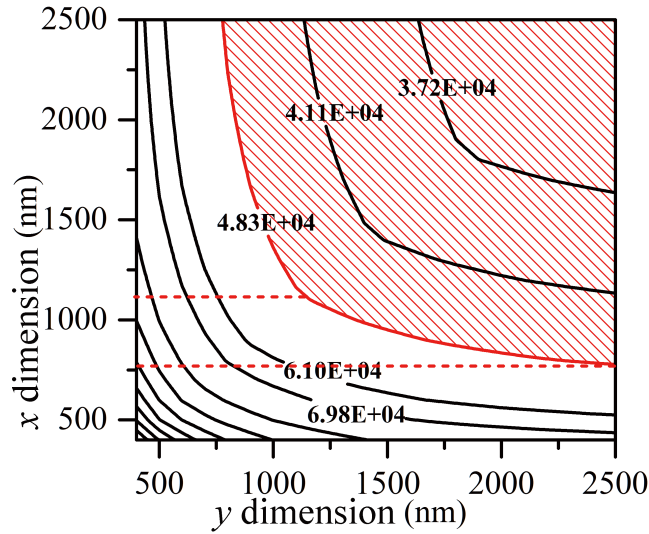

Figure 8 Contour showing the thermal resistance (K/W) against the width and length of gold wires with both the length and width varying.

The advantage of the topography-free sample is that thermal signals at the edge of the pattern can be obtained without topographically induced artifacts. This can be used to create another measurement of SThM probe-sample effective contact radius. A schematic of this measurement, shown in Figure 9 (a), illustrates the two scenarios where the probe is completely in contact with the SiN_x or gold as separated by a distance D. When a SThM probe moves from the SiN_x onto the gold, the transition of the thermal response is not an abrupt change but a ramp. This phenomenon can be the result of several factors. It has been proposed in other work[5,29,46] that for hard materials it is reasonable to treat the contact size as independent of material. We can therefore state that the transition of a circular contact across an abrupt thermal feature dictates this ramp. More specifically, the ramp results from the difference in probe-sample thermal interfacial resistance during this transition, as well as the nonuniformity of thermal resistance of the gold wire along its length from edge to centre.

Employing the same analysis described for the gold pad above, the thermal interfacial resistance between the probe and SiN_x has been determined to be 1.25×10^6 K/W, and that between the probe and gold as 0.985×10^6 K/W. This leads to an interesting observation: this difference alone would be enough to generate strong thermal contrast during a SThM scan, even if both materials had the same thermal conductivity.

We can now consider the effect of probe contact position on the gold wire. As already described, we can model the thermal resistance of the gold wire by treating it as a combination of a radial fin with the heat source at the centre and two straight fins of equal length. Following this, we can state that the thermal resistance will vary with position on the wire due to the differing ratio of the length for the two fins. As shown in Figure 9 (b), when a probe is in contact near the edge of a wire, we can divide the model into three sections. Section I is still a radial fin as described previously, with diameter equal to the width of the wire. Sections II and III are two straight fins separated by the contact point with length e and (L-e). This configuration necessitates only slight changes to the thermal model, specifically a revised value of "h_c" at the edge of the radial fin. This can obtained from eqn (7) by substituting $R_{straight}$ with the thermal resistance of the two straight fins in parallel.
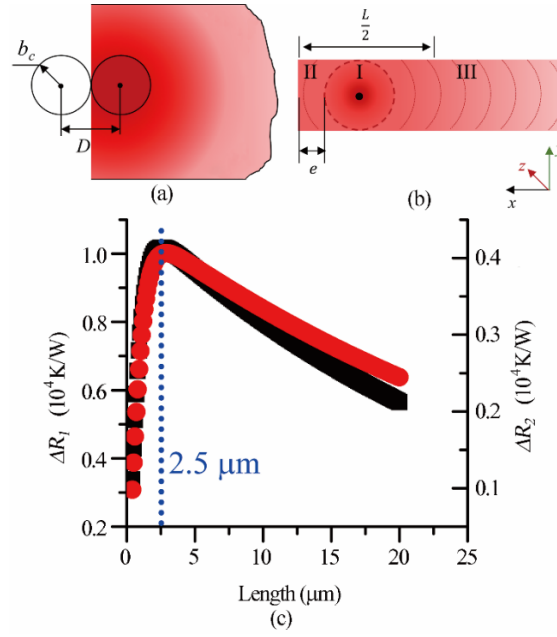
Figure 9 (a) Principle of the effective contact radius measurement. (b) Schematic of a probe in contact with a gold wire away from the centre. (c) Plots of thermal resistance difference between the probe contacting the edge and centre of the gold wire. R_1 is for a 200 nm wide wire (black squares) and R_2 is for a 400 nm wide wire (red circles).

The difference in modelled thermal resistance for the probe contacting the very edge and centre of the gold wire is given by ΔR. Figure 9 (c) shows ΔR varying with length of 200 nm and 400 nm wide wires. It can be clearly seen that the maximum variation occurs when the length is 2500 nm. It can also be seen that, even for 2500 nm long wires, there is only $\sim 1 \times 10^4$ K/W variation as the probe moves from the centre of the wire to the edge. This is comparable to the ideal maximum sensitivity of the probe, 1.41×10^4 K/W, as defined previously. Therefore, we can conclude that any probe temperature change is dominated by the transition from one contact material to the other, and hence $D = 2b_c$.
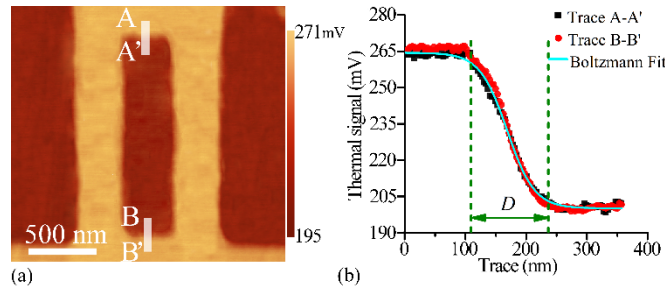

Figure 10 (a) Thermal image of a gold wire with two traces (A-A' and B-B') at top and bottom edges, and (b) plots of the thermal response for these two traces against scan length, with a Boltzmann fit.

This simplifies the determination of effective contact size between the probe and the sample through analysis of the thermal image. Figure 10 shows the thermal response signals from two line traces at the top (A-A') and the bottom (B-B') edges of the wire in Figure 10 (a). These traces are then plotted against the length of trace as shown in Figure 10 (b). Both traces are 18-pixels wide. The ramp region of the thermal signal is $D \approx 120$ nm, which gives the radius of effective contact area as ~ 60 nm. A simple description for the thermal spatial resolution of SThM in air can be obtained from the full width of half maximum (FWHM) of the trace using a Boltzmann sigmoidal fit[47,48]: $f(y) = y_2 + (y_1 - y_2)/(1 + e^{(x-x_0)/\Delta x})$. This gives an estimation of thermal-spatial resolution of $2 \times \Delta x = 45$ nm, which compares well with the value obtained using the same probe in other work and agrees with the observation that the radius of the probe limits the thermal spatial resolution[11,34,49] as this dictates contact radius to a large extent.

Conclusion

SThM is increasingly being used to measure material thermal properties at the nano-scale. However, it is sometimes overlooked that the thermal resistance of an object is a function of both its thermal conductivity and geometry. This fact is as true at the nano-scale as it is for much larger objects. In this work we present SThM measurements of nanoscale objects, clearly illustrating their changing thermal resistance as a function of geometry, even though the material system remains constant. The effect is strong, with the measured thermal contrast of a short gold wire being equivalent to a material having a thermal conductivity over twenty times smaller than the true value. Using this data we describe a new heat transfer combined fin (CF) model that allows the determination of sample thermal resistance, as measured by SThM, when the sample's dimensions fall in the intermediate regime between those of a nanoscopic contact area and a half space. This model accounts for the multi-dimensional thermal conduction within the thin film, as well as the thermal interface and the thermal spreading resistances intrinsic in the interaction between a SThM probe and sample.

The model was validated using experimental results obtained from SThM scans of topography-free, lithographically gold features with a range of geometries and boundary conditions. Both the model and experimental results demonstrate that the dimensions and boundary conditions of a rectangular thin film significantly affect its thermal resistance. This clearly illustrates the necessity to consider sample geometry when extracting material thermal properties from thermal resistance as measured using SThM. The model also shows that a SThM scan over the edge of an abrupt, topography free object can be used to estimate the effective contact radius and thermal-spatial resolution of a probe.

Finally, a combination of the CF model with a previously published lumped system model[30] can be used to interpret experiments obtained under ambient conditions using micromachined SiN_x SThM probes. This identifies the heat flux sensitivity of the system employed to be ~ 200 nW.

Acknowledgements

Notes and references

(1)   Majumdar, A. Scanning Thermal Microscopy. *Annu. Rev. Mater. Sci.* **1999**, *29*, 505–585.
(2)   Wielgoszewski, G.; Gotszalk, T. Scanning Thermal Microscopy (SThM): How to Map Temperature and Thermal Properties at the Nanoscale. In *Advances in Imaging and Electron Physics*; Hawkes, P. W., Ed.; Elsevier Inc.: London, 2015; Vol. 190, pp. 177–221.
(3)   Menges, F.; Mensch, P.; Schmid, H.; Riel, H.; Stemmer, A.; Gotsmann, B. Temperature Mapping of Operating Nanoscale Devices by Scanning Probe Thermometry. *Nat. Commun.* **2016**, *7*, 10874.
(4)   Chung, J.; Kim, K.; Hwang, G.; Kwon, O.; Choi, Y. K.; Lee, J. S. Quantitative Temperature Profiling through Null-Point Scanning Thermal Microscopy. *Int. J. Therm. Sci.* **2012**, *62*, 109–113.
(5)   Assy, A.; Gomès, S. Heat Transfer at Nanoscale Contacts Investigated with Scanning Thermal Microscopy. *Appl. Phys. Lett.* **2015**, *107*, 043105.
(6)   Hinz, M.; Marti, O.; Gotsmann, B.; Lantz, M. A.; Dürig, U. High Resolution Vacuum Scanning Thermal Microscopy of HfO2 and SiO2. *Appl. Phys. Lett.* **2008**, *92*, 043122.
(7)   Menges, F.; Riel, H.; Stemmer, A.; Dimitrakopoulos, C.; Gotsmann, B. Thermal Transport into Graphene through Nanoscopic Contacts. *Phys. Rev. Lett.* **2013**, *111*, 205901.
(8)   Kim, K.; Jeong, W.; Lee, W.; Sadat, S.; Thompson, D.; Meyhofer, E.; Reddy, P. Quantification of Thermal and Contact Resistances of Scanning Thermal Probes. *Appl. Phys. Lett.* **2014**, *203107*.
(9)   Menges, F.; Riel, H.; Stemmer, A.; Gotsmann, B. Quantitative Thermometry of Nanoscale Hot Spots. *Nano Lett.* **2012**, *12*, 596–601.
(10)   Fletcher, P. C.; Lee, B.; King, W. P. Thermoelectric Voltage at a Nanometer-Scale Heated Tip Point Contact. *Nanotechnology* **2011**, *23*, 035401.
(11)   Puyoo, E.; Grauby, S.; Rampnoux, J. M.; Rouvire, E.; Dilhaire, S. Thermal Exchange Radius Measurement: Application to Nanowire Thermal Imaging. *Rev. Sci. Instrum.* **2010**, *81*, 2–6.
(12)   Gomès, S.; Assy, A.; Chapuis, P. Scanning Thermal Microscopy: A Review. *Phys. status solidi* **2015**, *212*, 477–494.
(13)   Shi, L.; Majumdar, A. Thermal Transport Mechanisms at Nanoscale Point Contacts. *J. Heat Transfer* **2002**, *124*, 329.
(14)   Kim, K.; Chung, J.; Won, J.; Kwon, O.; Lee, J. S.; Park, S. H.; Choi, Y. K. Quantitative Scanning Thermal Microscopy Using Double Scan Technique. *Appl. Phys. Lett.* **2008**, *93*, 203115.
(15)   Assy, A.; Lefèvre, S.; Chapuis, P. O.; Gomès, S. Analysis of Heat Transfer in the Water Meniscus at the Tip-Sample Contact in Scanning Thermal Microscopy. *J. Phys. D. Appl. Phys.* **2014**, *47*, 442001.
(16)   Assy, A.; Gomès, S. Temperature-Dependent Capillary Forces at Nano-Contacts for Estimating the Heat Conduction through a Water Meniscus. *Nanotechnology* **2015**, *26*, 355401.
(17)   Puyoo, E.; Grauby, S.; Rampnoux, J.-M.; Rouvière, E.; Dilhaire, S. Scanning Thermal Microscopy of Individual Silicon Nanowires. *J. Appl. Phys.* **2011**, *109*, 024302.
(18)   Shi, L.; Zhou, J.; Kim, P.; Bachtold, A.; Majumdar, A.; McEuen, P. L. Thermal Probing of Energy Dissipation in Current-Carrying Carbon Nanotubes. *J. Appl. Phys.* **2009**, *105*, 10–15.
(19)   Hwang, G.; Kwon, O. Measuring the Size Dependence of Thermal Conductivity of Suspended Graphene Disks Using Null-Point

Scanning Thermal Microscopy. *Nanoscale* **2016**, *8*, 5280–5290.

(20) Chen, S.; Moore, A. L.; Cai, W.; Suk, J. W.; An, J.; Mishra, C.; Amos, C.; Magnuson, C. W.; Kang, J.; Shi, L.; *et al.* Raman Measurements of Thermal Transport in Suspended Monolayer Graphene of Variable Sizes in Vacuum and Gaseous Environments. *ACS Nano* **2011**, *5*, 321–328.

(21) Chiang, T. Y.; Banerjee, K.; Saraswat, K. C. Analytical Thermal Model for Multilevel VLSI Interconnects Incorporating via Effect. *IEEE Electron Device Lett.* **2002**, *23*, 31–33.

(22) Chen, Z.; Lin, Y.-M.; Rooks, M. J.; Avouris, P. Graphene Nano-Ribbon Electronics. *Phys. E Low-dimensional Syst. Nanostructures* **2007**, *40*, 228–232.

(23) Yang, N.; Zhang, G.; Li, B. Thermal Rectification in Asymmetric Graphene Ribbons. *Appl. Phys. Lett.* **2009**, *95*, 033107.

(24) Ftouni, H.; Blanc, C.; Tainoff, D.; Fefferman, A. D.; Defoort, M.; Lulla, K. J.; Richard, J.; Collin, E.; Bourgeois, O. Thermal Conductivity of Silicon Nitride Membranes Is Not Sensitive to Stress. *Phys. Rev. B* **2015**, *92*, 125439.

(25) Tang, H.; Xiong, Y.; Zu, F.; Zhao, Y.; Wang, X.; Fu, Q.; Jie, J.; Yang, J.; Xu, D. Length-Dependent Thermal Transport in One-Dimensional Self-Assembly of Planar π-Conjugated Molecules. *Nanoscale* **2016**, *8*, 11932–11939.

(26) Yovanovich, M. M. Conduction and Thermal Contact Resistance (Conductance). In *Handbook of Heat Transfer*; Rohsenow, W. M.; Hartnett, J. P.; Cho, Y. I., Eds.; McGraw-Hill: New York, 1998; pp. 111–183.

(27) Yovanovich, M. M.; Muzychka, Y. S.; Culham, J. R. Spreading Resistance of Isoflux Rectangles and Strips on Compound Flux Channels. *J. Thermophys. Heat Transf.* **1999**, *13*, 495–500.

(28) Soudi, A.; Dawson, R. D.; Gu, Y. Quantitative Heat Dissipation Characteristics in Current-Carrying GaN Nanowires Probed by Combining Scanning Thermal Microscopy and Spatially Resolved Raman Spectroscopy. *ACS Nano* **2011**, *5*, 255–262.

(29) Ge, Y.; Zhang, Y.; Weaver, J. M. R.; Zhou, H.; Dobson, P. S. Topography-Free Sample for Thermal Spatial Response Measurement of Scanning Thermal Microscopy. *J. Vac. Sci. Technol. B, Nanotechnol. Microelectron. Mater. Process. Meas. Phenom.* **2015**, *33*, 06FA03.

(30) Ge, Y.; Zhang, Y.; Booth, J. A.; Weaver, J. M. R.; Dobson, P. S. Quantification of Probe–sample Interactions of a Scanning Thermal Microscope Using a Nanofabricated Calibration Sample Having Programmable Size. *Nanotechnology* **2016**, *27*, 325503.

(31) Ge, Y.; Zhang, Y.; Booth, J. B.; Weaver, J. M. R.; Dobson, P. S. Quantification of Probe-Sample Interactions of a Scanning Thermal Microscope Using a Nanofabricated Calibration Sample Having Programmable Size. *Nanotechnology Accepted*.

(32) Pettes, M.; Shi, L. A Reexamination of Phonon Transport Through a Nanoscale Point Contact in Vacuum. *J. Heat Transfer* **2013**, *136*, 032401.

(33) Zhang, Y.; Dobson, P. S.; Weaver, J. M. R. High Temperature Imaging Using a Thermally Compensated Cantilever Resistive Probe for Scanning Thermal Microscopy. *J. Vac. Sci. Technol. B* **2012**, *30*, 010601.

(34) Tovee, P.; Pumarol, M.; Zeze, D.; Kjoller, K.; Kolosov, O. Nanoscale Spatial Resolution Probes for Scanning Thermal Microscopy of Solid State Materials. *J. Appl. Phys.* **2012**, *112*, 114317.

(35) Bodzenta, J.; Juszczyk, J.; Chirtoc, M. Quantitative Scanning Thermal Microscopy Based on Determination of Thermal Probe Dynamic Resistance. *Rev. Sci. Instrum.* **2013**, *84*.

(36) Holman, J. P. *Heat Transfer*; 10th ed.; McGraw-Hill: New York, 2010.

(37) Gotsmann, B.; Lantz, M. A.; Knoll, A.; Dürig, U. Nanoscale Thermal and Mechical Interactions Studied Using Heatable Probes. In *Nanotechnology*; Fuchs, H., Ed.; Wiley-VCH: Weinheim, 2009; Vol. 6, pp. 121–169.

(38) Schmidt, A. J.; Cheaito, R.; Chiesa, M. Characterization of Thin Metal Films via Frequency-Domain Thermoreflectance. *J. Appl. Phys.* **2010**, *107*, 024908.

(39) Zhang, X.; Grigoropoulos, C. P. Thermal Conductivity and Diffusivity of Free-Standing Silicon Nitride Thin Films. *Rev. Sci. Instrum.* **1995**, *66*, 1115–1120.

(40) Smith, A. N.; Hostetler, J. L.; Norris, P. M. THERMAL BOUNDARY RESISTANCE MEASUREMENTS USING A TRANSIENT THERMOREFLECTANCE TECHNIQUE. *Microscale Thermophys. Eng.* **2000**, *4*, 51–60.

(41) Stevens, R. J.; Smith, A. N.; Norris, P. M. Measurement of Thermal Boundary Conductance of a Series of Metal-Dielectric Interfaces by the Transient Thermoreflectance Technique. *J. Heat Transfer* **2005**, *127*, 315.

(42) Yang, J.; Ziade, E.; Schmidt, A. J. Uncertainty Analysis of Thermoreflectance Measurements. *Rev. Sci. Instrum.* **2016**, *87*, 014901.

(43) Nelson, B.; King, W. Modeling and Simulation of the Interface Temperature Between a Heated Silicon Tip and a Substrate. *Nanoscale Microscale Thermophys. Eng.* **2008**, *12*, 98–115.

(44) Gundrum, B. C.; Cahill, D. G.; Averback, R. S. Thermal Conductance of Metal-Metal Interfaces. *Phys. Rev. B* **2005**, *72*, 245426.

(45) Wielgoszewski, G.; Sulecki, P.; Gotszalk, T.; Janus, P.; Szmigiel, D.; Grabiec, P.; Zschech, E. Microfabricated Resistive High-Sensitivity Nanoprobe for Scanning Thermal Microscopy. *J. Vac. Sci. Technol. B* **2010**, *28*, C6N7.

(46) Gotsmann, B.; Lantz, M. A. Quantized Thermal Transport across Contacts of Rough Surfaces. *Nat. Mater.* **2012**, *12*, 59–65.

(47) Tovee, P. D.; Kolosov, O. V. Mapping Nanoscale Thermal Transfer in-Liquid Environment-Immersion Scanning Thermal Microscopy. *Nanotechnology* **2013**, *24*, 465706.

(48) Kiracofe, D.; Raman, A. Nonlinear Dynamics of the Atomic Force Microscope at the Liquid-Solid Interface. *Phys. Rev. B* **2012**, *86*, 205405.

(49) Pumarol, M. E.; Rosamond, M. C.; Tovee, P.; Petty, M. C.; Zeze, D. A.; Falko, V.; Kolosov, O. V. Direct Nanoscale Imaging of Ballistic and Diffusive Thermal Transport in Graphene Nanostructures. *Nano Lett.* **2012**, *12*, 2906–2911.